ADVANCED FUNCTIONAL MATERIALS
www.afm-journal.de

Materials Views
www.MaterialsViews.com

Broadband Omnidirectional Diversion of Light in Hybrid Plasmonic-Photonic Heterocrystals

*Boyang Ding, Maria Bardosova, Martyn E. Pemble, Alexander V. Korovin, Ulf Peschel, and Sergei G. Romanov**

Broadband, omnidirectional, and polarization-independent diversion has been achieved of more than 90% of the light flow intensity off its incidence direction using hybrid metal–dielectric plasmonic-photonic heterocrystals. These architectures were prepared by depositing metal film on the interface between two photonic crystals of different parameters. The magnitude of light losses was extracted from angle-resolved measurements of transmission and reflectance spectra. Comparing these data for different stages of constructing the complex architecture, the diffraction in colloidal crystals, the excitation and radiative decay of short-living surface plasmon polaritons in a corrugated metal film and the eigenmode mismatch at the interface between two different photonic crystals were identified as corroborating physical mechanisms behind the light diversion.

1. Introduction

Light scattering,[1] which is conventionally considered as an undesirable phenomenon in optical materials, can be a specific target for photovoltaics, comfortable and energy efficient lighting, random lasing and sensing. The important parameters are then the spectral interval and the efficiency of scattering. Scattering in randomly disordered media occurs at a length scale much longer compared to a wavelength. This statement applies to all methods exploiting the principles of geometrical optics for diverting the propagating light. To break this rule non-trivial photon management systems are required. Towards this aim a number of solutions based on the wave optics in photonic crystals (PhCs)[2] and photon-to-plasmon coupling in metal-dielectric structures have been suggested.[3]

Recent interest to this topic was boosted by introduction of thin-film light harvesting materials, where the increase of the dwell time of photons in absorbing medium is necessary to promote the photon absorption. A design target for this application is achieving the abrupt change of the beam propagating direction within the path length as short as, ideally, a fraction of wavelength. Motivated by this challenge we explored the light scattering in the recently emerged hybrid metal-dielectric PhCs.[4]

In PhCs, which are the periodically arranged ensembles of light scatterers, the diffraction mechanism provides expansion of a light beam in several propagation directions. In three-dimensional (3D) PhCs the interference of scattered waves allows to reduce the length path necessary for the beam diversion down to 2–3 times the wavelength.[2,5,6] The shortcoming of this approach is a strict correlation between the wavelength and direction of a diverted beam. Hence, to achieve a quasi-continuous diversion one should relay on the diffraction at high-index crystal planes. In 3D PhC this means at least doubling the unit cell size compared the wavelength of diffracted light. However, if only a narrow bandwidth is required, then it is possible to pattern the thin, down to 100 nm, layer of absorbing material as a 2D PhC and use it for diffractive light coupling to a planar waveguide.[7–9]

Alternatively, the PhC can be almost isolated from coupling to the free space that increases the light path lengths in PhC volume above the Yablonovitch limit. Such so-called ultra light trapping can be achieved by restricting the trap acceptance angle to a narrow cone along the one particular direction.[10,11] Unfortunately, this approach is associated with rejection of both the oblique incident and diffuse light. In addition, the crystalline quality of the PhC lattice for use in such trap should be very high.

PhC traps can also use light coupling to the localized photon states of artificial defects. Such localized states act as high-quality resonators, i.e., they force light to bouncing in a tiny space. Alternatively, the slowly propagating light that is coupled to flat photonic bands in the photonic band gap (PBG) structure also provides the increase of the dwell time of photons. These mechanisms enable greater overall absorption of light than

Dr. S. G. Romanov
Institute of Optics
Information and Photonics
University of Erlangen-Nuremberg
Günther-Scharowsky-Str.1, 91058 Erlangen, Germany
E-mail: Sergei.Romanov@mpl.mpg.de
Dr. S. G. Romanov
Ioffe Physical Technical Institute RAS
194021, Polithekhnicheskaya ul., 26, St. Petersburg, Russia
B. Ding, Dr. M. Bardosova, Prof. M. E. Pemble
Tyndall National Institute
University College Cork
Lee Maltings, Prospect Row, Cork, Ireland
Dr. A. V. Korovin, Prof. U. Peschel
Institute of Optics
Information and Photonics
University of Erlangen-Nuremberg
Günther-Scharowsky-Str.1, 91058 Erlangen, Germany

DOI: 10.1002/adfm.201100695

 © 2011 WILEY-VCH Verlag GmbH & Co. KGaA, Weinheim

mechanisms based on geometrical ray optics,[12] but, typically, over a narrow spectral range.

Turning now to the possible exploitation of plasmon resonances in light traps, two scenarios can be highlighted.[13,14] First one exploits the fact that scattering and absorption cross sections at the resonance frequency of plasmon oscillations that are localized in a metallic nanoparticle greatly exceed the particle size.[15] However, spectral tuning of localized plasmon resonances requires to exert some degree of control on the size and mutual positioning of the particles, which represents a significant technological challenge.[16]

The second scenario relies on surface plasmon polaritons (SPPs) propagating along the metal-dielectric interface.[17] The SPP excitation requires application of a special coupling structure[18–20] in order to match the photon and SPP wavevectors. Once SPPs are excited they can uptake a sizable, up to 95%,[21] fraction of incident light intensity, providing strong field localization in the guided interface mode and, hence, a large amplitude of the electromagnetic (EM) field in the near-field zone. These modes can propagate for several micrometers without substantial loss and then dissipate in the metal or decay radiatively. As the result, the absorption in an adjacent absorbing semiconductor can be greatly enhanced.[22] In terms of the operating spectral band, the grating couplers with small number of grooves are less frequency selective. In fact, a single scattering object, such as a ridge or a groove in a metallic film, can act as a relatively efficient broadband coupler.[22]

A 1D thin metal film grating attached to a planar semiconductor waveguide provides increased scattering of incident light into propagating modes due to multiple reflections at the frequencies of Fabry–Perot oscillations within the film and enhanced light coupling into guided modes at the SPP resonance frequency. At these resonances the absorption and scattering cross sections of each grating element will be at maximum[23] Obviously, the typical shortcoming of SPP-based optical structures, namely, the poor handling of the light with polarization that is perpendicular to the plane of incidence, remains in effect in such structures.

If the PhC- and plasmonic-based trap structures are both built to increase the dwell time of optical excitations and to route the incoming light for in-plane propagation, the convergence of these approaches can improve the trap performance.[24–27]

The self-organized colloidal crystals, the opals, assembled from equal-size dielectric spheres,[28] possess the properties of 3D PhCs. Their use, e.g., in telecommunications, have thus far been prohibited by insufficient lattice regularity, but they can be considered for applications that are less demanding with respect to frequency selection. For example, the enhancement of light harvesting efficiency has been demonstrated in tandem solar cell with inverted Si opals[29] and ZnO opals[30] operating as an intermediate reflector. Also, inverted TiO_2 opals were used as Bragg mirrors in dye-sensitized solar cells.[31–33]

Recently, we used photonic heterocrystals to demonstrate the specific scattering mechanism that is based on coupling losses occurring at the interface between PhCs with different topologies[34] (**Figure 1**a). The attractive features of this approach are (i) positioning of the source of scattered light in depth of the structure, so that the scattered light ought to traverse the structure before leaving it and (ii) the incoherent character of the scattering. The aim of the present work is to enhance the scattering in the heterocrystals by coupling photons to SPPs in a thin metal film, which is deposited on the interface between different PhCs (Figure 1b).

Naturally, the metal film coating on the opal template replicates the surface profile of the monolayer of closely assembled spheres,[35] i.e., it forms 2D metal diffraction grating or 2D plasmonic crystal[36] (Figure 1c). It is well known that SPPs can be excited in periodically profiled metal films due to diffractive light coupling.[37,38] In the hybrid crystal the incoming wave will be coupled to both the Bloch modes of PhC and to the SPPs of a plasmonic crystal.[39] The matching periodicity of these EM crystals ensures the interaction between plasmonic and photonic modes[4] and, on top, this interaction gives rise to hybrid modes.[35,40]

In a naive description, the incident light is, at first, diverted by diffraction in the 3D PhC lattice off the incident direction and off the plane of light incidence and, consequently, these diffraction orders approach the periodically corrugated metal film, where they excite SPPs. Consequently, SPPs transfer EM energy along the metal film. Fortunately, SPPs can be forced to decay radiatively by the scattering potential provided by the PhC of another periodicity that is placed in the near-field zone of a metal film (Figure 1b,d). Since both the diffraction in PhCs and the excitation/decay of SPPs are associated with changing the directions of the EM wave propagation, the incident radiation should finally criss-cross the volume of the hybrid structure. The deterministic character of this light diversion mechanism allows to adjust the maximum of diversion efficiency to a desirable frequency interval by changing the lattice period of the opal crystal.

2. Light Diversion in the Bare Opal Film

In order to establish the reference and provide the definitions we consider first the planar thin opal film. The 'losses', L, of the intensity of incident light, I, were adopted as the measure of the light diversion from the zero diffraction order (this order propagates along the incidence direction) to allow the comparison between different structures. The losses, $L = I - T - R$, balance the intensities of the incident, zero-order reflected (R) and zero-order transmitted (T) light. In the case of a bare opal film assembled from dielectric spheres, the losses are equal to the intensity of the light flow that is diverted off the incidence direction by non-zero-order diffraction and scattering because of negligibly small absorption.

The reflectance and transmission spectra of the opal film under s-polarized light were obtained at different angles of light incidence (**Figure 2**a,b). Correspondingly, we can estimate losses at any angle (Figure 2c,d). Similar loss spectra were obtained in p-polarized light.

There are several diffraction resonances in the opal lattice that appear in reflectance and transmission spectra as maxima and minima, respectively. The resonance centered at 1265 nm for normal light incidence relates to the diffraction at (111) planes of the face centered cubic (fcc) lattice, which satisfactorily approximates the symmetry of the opal crystal.[41] Bragg law fit to its dispersion was used to estimate the sphere diameter

© 2011 WILEY-VCH Verlag GmbH & Co. KGaA, Weinheim

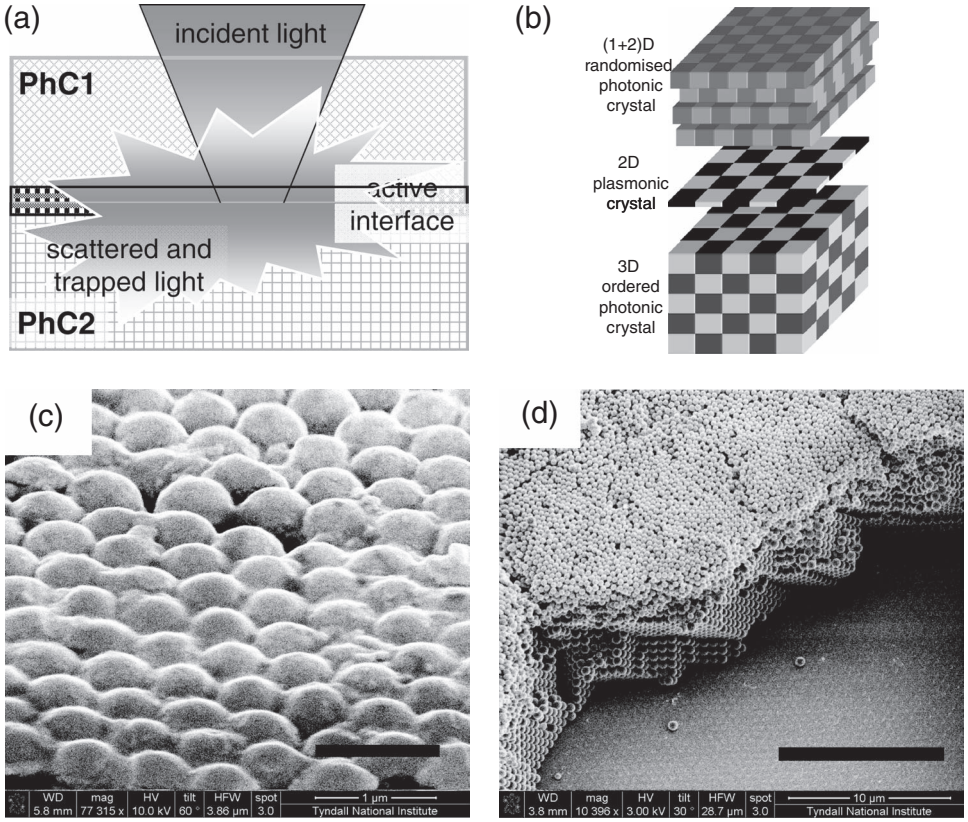

Figure 1. a) The idea of light scattering at the active interface in the photonic heterocrystal that involves scattering due to mode mismatch between two PhCs and light-to-SPP coupling. b) Schematics of studied architecture: two PhCs, one of which can be the intentionally randomized, and the corrugated metal film (2D slab plasmonic crystal) at the interface between them. c) SEM image of the 50 nm thick Au coating on top of the opal crystal. The scale bar is 1 μm. d) SEM image of the hybrid heterocrystal composed from the opal crystal assembled on a glass substrate, the spattered Au film and the Langmuir-Blodgett colloidal crystal deposited on top of a metal film. The scale bar is 10 μm.

D_O = 560 nm and the effective index of refraction of the opal film n_{effO} = 1.37. Then the dispersions of other diffraction resonances (Figure 2a) were calculated using the Bragg law for the fcc lattice. The thickness of this opal film, ~7 μm, was obtained from the periodicity of Fabry-Perot oscillations using the n_{effO} estimate.

This opal film diverts up to 85% of the incident light intensity in the spectral range $\lambda \leq D_O$ (Figure 2c). Comparison with

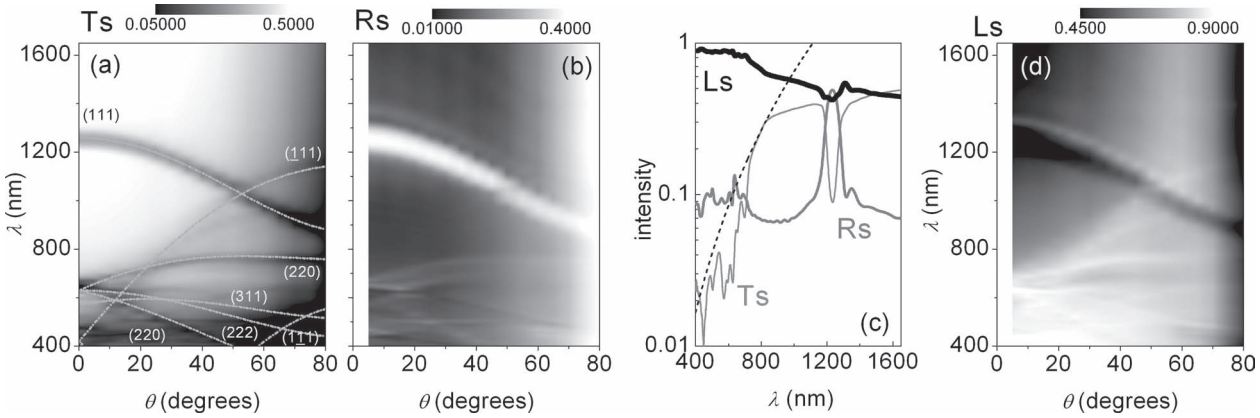

Figure 2. a) The transmission and b) reflectance spectra of the bare opal film under s-polarized light illumination. The lines in the panel (a) show the dispersion of diffraction resonances occurring in the fcc lattice of the lattice constant and effective index of refraction adopted from the opal lattice. Numbers at curves indicate the (*hkl*) indices of diffracting lattice planes. c) The transmission (Ts, thin line), reflectance (Rs, thicker line) and loss (Ls, thick line) spectra obtained under the s-polarized light illumination of the bare opal film at θ = 15°. Dashed line corresponds to the transmission trend in the case of diffuse light scattering (Rayleigh law). The Rayleigh fit was adjusted to the experimental level of transmission at 800 nm. d) The loss pattern obtained from spectra in panels (a,b).

© 2011 WILEY-VCH Verlag GmbH & Co. KGaA, Weinheim

Rayleigh scattering that changes like $1/\lambda^4$ shows that transmission drops even faster than it would be expected in the case of diffuse scattering at the lattice irregularities. This sudden drop is associated with the coherent scattering to the diffraction orders of high-index crystal planes, which are closely spaced in this spectral range and propagate off the incidence direction. Hence, the losses in this spectral range correspond to deterministic re-routing of the incident light intensity.

The loss pattern obtained in s-polarized light undoubtedly shows that losses start to grow in register with the onset of diffraction resonances at high-index planes of the opal lattice, namely, at ~700 nm, and follow the dispersion of these resonances with increasing incidence angle (Figure 2d). Moreover, at $\theta > 50^{\circ}$ the range of high losses extends to the near infrared because the path length of incident beam inside the opal film rapidly increases. At grazing incidence the ballistic regime of the light propagation (the light beam experiences no scattering) concedes to the diffuse one due to random scattering at opal defects. This conversion also applies to the diffraction orders, the lateral propagation of which approaches the angle of total internal reflection at the opal-air interface. Thus, two loss mechanisms cooperate in the bare opal film: i) coherent scattering to diffraction orders of high-index planes and ii) diffuse scattering of the incident beam and its diffraction orders[42] (**Figure 3**). The polarization dependence of light transport in opals is reasonably weak at frequencies away from diffraction resonances.[43] Certainly, the opal film itself is not very efficient in light diversion because of 10% strong reflectance in the range $\lambda < n_{\mathrm{effO}} D_{\mathrm{O}}$ and 50% high reflectance at the (111) resonance.

3. Light Losses in the Langmuir-Blodgett Au-Opal Hybrid Architecture

Deliberate complicating of the light traffic was achieved by assembling a hetero-PhC from two PhCs with different lattice symmetries and depositing a thin Au film on the interface between these crystals. In order to make the light coupling from one PhC to another even more difficult, we used PhCs of different topology, namely, the 3D opal crystal self-assembled from 560 nm PMMA spheres and the (2 + 1)D Langmuir–Blodgett (LB) crystal force-assembled from 350 nm SiO_2 spheres (Figure 1b,d).

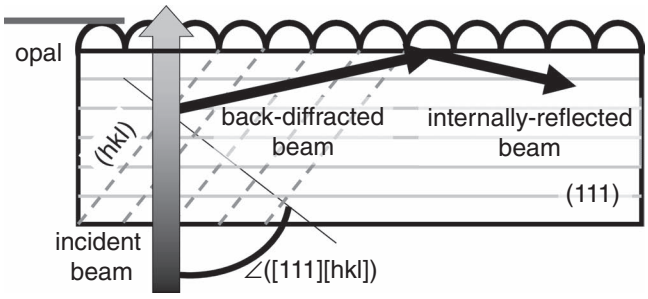

Figure 3. Schematics illustrating the diffraction of the incident light in the PhC lattice using the example of the normally incident beam, which is back-diffracted at the (*hkl*) plane. While this incident beam propagates ballistically, the diffracted beam will be eventually scattered at opal defects. Opal surface is shown by semicircles.

The transmission, reflectance and loss spectra of the LB-Au-opal hybrid are shown in **Figure 4** in a manner allowing a comparison to that of the bare opal film (Figure 2c). The reflectance spectra of LB- and opal-sides of the LB-Au-opal sample differ from each other being dominated either by the diffraction resonance at the stack of (111) planes in the opal or by the diffraction at the stack of monolayers composing the LB film. The latter resonance appears as a peak in the reflectance spectrum at 758 nm, but its intensity is only ~5% at the maximum (Figure 4a), whereas the former is almost the same as in the bare opal. The presence of the metal film in a hybrid provides the higher, compared to that in a bare opal, off-resonance reflection background on which the diffraction resonances are superimposed. The transmission spectrum is invariant with respect to the sequence of hybrid components traversed by a light beam. Correspondingly, two loss spectra are obtained depending on the side of the sample, which is exposed to illumination (Figure 4a).

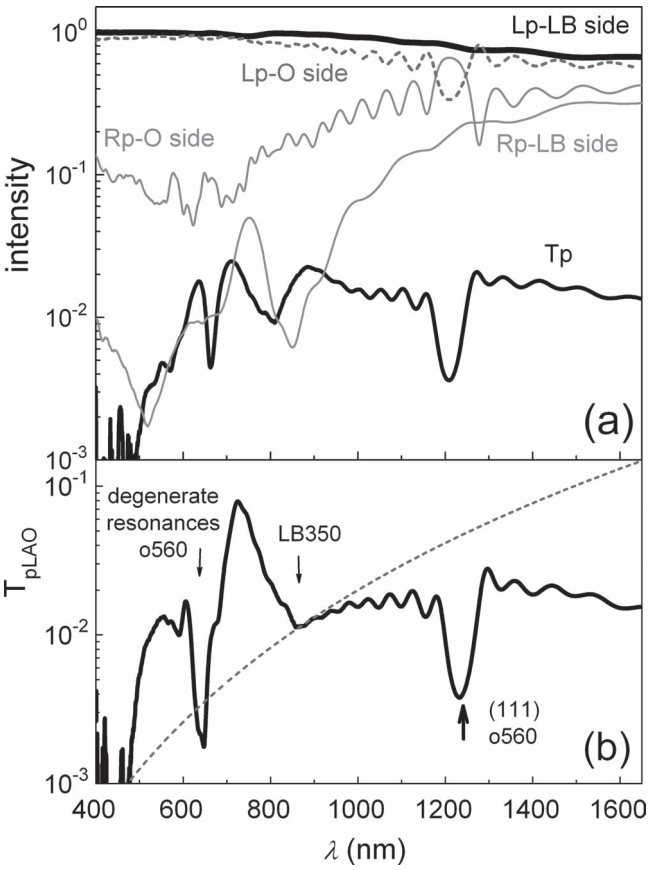

Figure 4. a) The loss spectra of the LB-Au-opal-glass hybrid structure obtained at $\theta = 15^{\circ}$ from the transmission (Tp) and reflectance (Rp) spectra under the p-polarized light for the illumination of the heterostructure from the LB and the opal crystal sides (labeled as Lp-LB side and Lp-O side, respectively. "O" stands for opal). Transmission spectrum does not change with reversing the direction of the probe beam from exposing either the O- or LB-side of this structure. b) Transmission of this heterostructure at $\theta = 0^{\circ}$ in comparison to the transmission prescribed by the Rayleigh law (dashed line).

© 2011 WILEY-VCH Verlag GmbH & Co. KGaA, Weinheim

The metal spattered on the opal surface acquires the shape of interconnected semi-shells having variable thickness, deep corrugation and through holes (Figure 1c).[35] This topology allows the efficient diffractive coupling of incident light to SPPs localized at the metal film surfaces. On the one hand, the reflectance of the metal film reduces the overall transmission of this hybrid. On the other hand, the SPPs at opposite sides of the corrugated and perforated metal film can tunnel through the film. One consequence of such tunneling is the extraordinary transmission,[37] which is seen as the transmission band in the spectra of LB-Au-opal hybrid with maximum transmission of 10% at 725 nm (Figure 4b). At $\theta = 0^{o}$ this transmission band overlaps the degenerate (200), (220), and (222) diffraction minima, thus shifted to ~650 nm (Figure 4b). As a result of SPP-related enhancement, the transmission of the hybrid mostly exceeds the projected Rayleigh-type trace at $\lambda < 850$ nm.

The LB-Au-opal hybrid acquires the milky appearance. This occurs due to light scattering, i.e., the light losses in the hybrid heterocrystal exceed those in the bare opal film. The almost overall 10-fold reduction of the LB-Au-opal transmission is responsible for the loss increase. (Figure 4a). Remarkably, substantially higher losses are detected if the LB side is illuminated, because the reflectance of the LB side of the hybrid is about order of magnitude lower compared to that of its opal side.

The difference in losses becomes clear, when loss patterns corresponding to opal- and LB-sides of this hybrid are compared (**Figure 5**). The magnitude of losses on excess of 90% for the LB-side is achieved at $\lambda < 1200$ nm for both light polarizations and for all incidence angles. The losses obtained when illuminating the opal side of the hybrid are lower in correspondence to higher reflectance of the opal film.

It is instructive to note that under the s-polarized light illumination, the long wavelength onset of high losses fits the (111) diffraction resonance in the opal crystal (Figure **5**a). In contrast, the loss pattern under the p-polarized illumination shows its long wavelength onset terminated by the dispersion of SPP modes (Figure 5b). This observation demonstrates (i) the cooperation of diffraction and plasmonic mechanisms in the light scattering in hybrid architectures and (ii) the connection of the diversion mechanism to the periodicity of the crystal.

Overall, the light diversion in a hybrid heterocrystal can be summarized as follows: (i), the intensity of losses in s- and p-polarized light are equalized, i.e., diversion becomes the polarization insensitive, (ii), the losses only weakly depend on the angle of light incidence, i.e., diversion becomes insensitive to this angle and (iii), the intensity of losses exceeds 90% at $\lambda < 1200$ nm and decreases smoothly to longer wavelengths.

4. Light Trapping and Light Absorption

Exploiting a metal film in a light scattering architecture raises a concern about light absorption, which is an intrinsic property of any dissipative component. Calculations show that the absorption of the planar 50-nm-thick Au film approaches ~2% at $\lambda = 900$ nm and increases to about 50% at $\lambda \approx 500$ nm due to interband transitions in the gold[44] (**Figure 6**). Experimental data for the flat film corroborate the calculated spectra.

Let us represent a hybrid heterocrystal as a 3-layer structure consisting of a planar 50 nm Au film sandwiched between two homogeneous dielectric films (**Figure 7**a), the refractive indices of the latter are chosen to be equal to n_{effO} and n_{effLB} (dashed line in Figure 7b). In this planar geometry the coupling device is necessary for exciting the SPPs by the incident light, hence, we used the prism of high index material on the left side of the model structure.

The EM field distribution across the structure was calculated using transfer matrix method. The magnitude of the Poynting vector representing the energy flux propagating in the plane of the 3-layer structure shows that the energy is coupled to SPPs

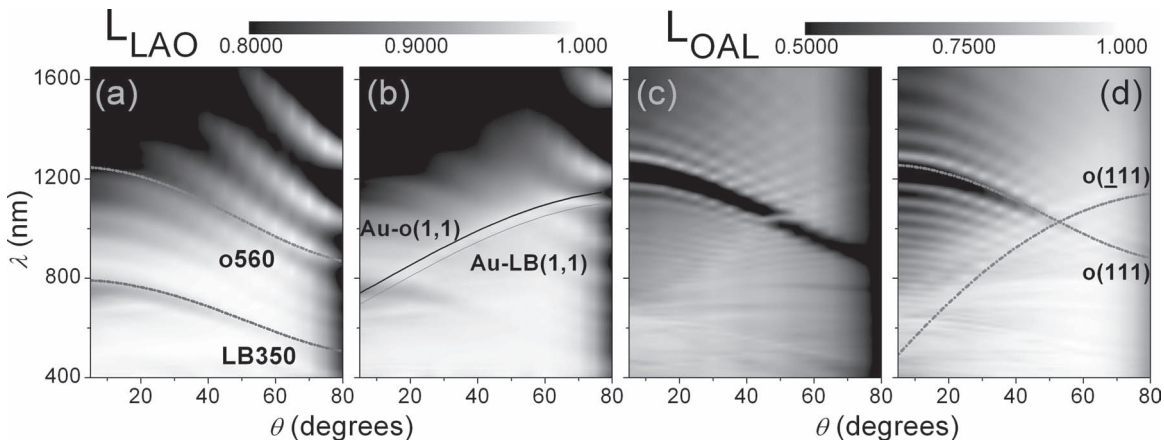

Figure 5. a,b) The loss patterns along the LB-Au-opal-glass (substrate) light path through the hybrid heterocrystal in the s- and p-polarized light, respectively. c,d) The same along the glass (substrate)-opal-Au-LB path. a) Dash-dotted lines depict the dispersion of major diffraction resonances in the opal and LB crystals. The diffraction at the stack of sphere monolayers in the LB film satisfies the Bragg law with parameters $D_{LB} = 350$ nm and $n_{effLB} = 1.28$. The dispersion of the (111) resonance in the opal part of the heterocrystal remains the same as in the single opal film (compare to Figure 2a). b) Thin and thick lines show the dispersion of the longest wavelength SPP modes in the hexagonal lattice (see Figure 9c for explanations) on the opal- and LB-sides of the Au film. The larger period of Fabry-Perot oscillations in panels (a,b) corresponds to the thinner LB film compared to (c,d) the shorter Fabry–Perot oscillations in the thicker opal film. This distinction occurs due to high reflectivity of the Au film that separates the opal film from the LB film.

© 2011 WILEY-VCH Verlag GmbH & Co. KGaA, Weinheim

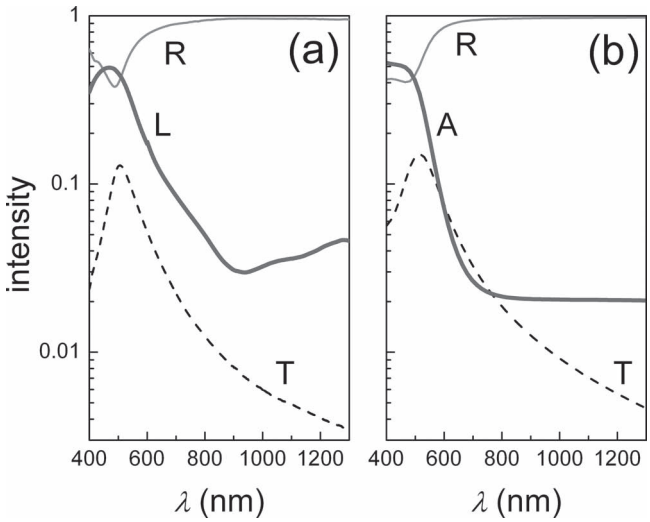

Figure 6. a) Experimental and b) calculated transmission (*T*), reflectance (*R*), loss (*L*) and absorption (*A*) spectra of the planar 50 nm Au film along the normal incidence.

(Figure 7b). It is instructive that SPP- transported electromagnetic energy (i) is confined in very close vicinity to the metal surface because its magnitude decays in depth of the dielectric at the length scale of a wavelength, (ii) propagates along the metal/dielectric interface and (iii) transforms about 95% of the intensity of incident light into SPPs if the Kretschmann coupling geometry is used.[21] Such scheme allows to re-direct the incident radiation along the film plane and to confine it in the middle of the hybrid structure. Thus, the trap function is achieved. Obviously, if the flat metal film is embedded in a dielectric host, the most of the SPP-coupled energy is dissipated in the metal and generates unwanted heat.

Since the corrugation is intrinsically embedded in opal-templated Au film, the diffractive coupling of light to SPPs is always in effect that makes no need in prism coupler. In this case about 80% of incident radiation can be transformed to SPPs.[21] Fortunately, the absorption in a corrugated metal film is much lower than in a flat film for following reasons: (i) the SPPs in Au-opal are strongly coupled to Bloch modes of PhC that gives rise to hybrid modes, which partially localized in the dielectric and experience less dissipation compared to SPPs of the free standing metal film[38] and (ii) the life time of SPPs becomes much shorter than their absorption time, because the depth of the metal film corrugation makes up to 50% of the corrugation period. If one would be targeting the long-range SPPs, this depth should not exceed 10% of the period.[45] We did not attempt to estimate the light absorption in such hybrid architecture due to complexity of the task, but, in the first approximation, we can neglect the dissipation of plasmon-polaritons in a metal film because SPPs are scattered back to light well before they might be absorbed.[38] Note, that this conclusion is invalid for the spectral range below 600 nm due to intrinsic absorption in a gold film.

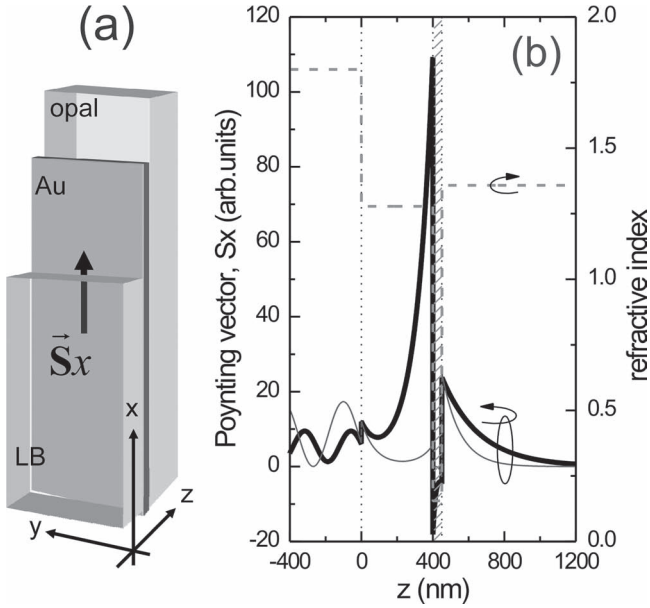

Figure 7. a) Schematics of the model 3-layer dielectric-metal-dielectric structure. $\vec{S}x$- is the x-component of the Poynting vector. b) $\vec{S}x$ distribution across the structure at $\lambda = 700$ nm for the SPPs localized at the effective LB (thick line) and effective opal (thin line) film sides of the Au film. The refractive index profile of the model structure is shown by the dashed line. Light coupling to SPP modes is provided by the prism of the index of 1.8 in the Kretschmann geometry that is attached to the LB-like dielectric film. The light impinges on the left side of a dielectric layer representing the LB film. The dotted line at $z = 0$ nm is the prism boundary. The complex refractive index of the Au film (at $z = 400$ nm) is shown by the shaded box.

5. Loss Enhancement by Metal Coating

It is instructive to explore the development of losses along building the hybrid heterocrystal up. Let us compare bare and Au-coated opals at first. If the metal-coated side is examined, the losses in the Au-opal hybrid exceed that in the bare opal film only in a specific spectral interval and for a limited range of incident light angles (**Figure 8**a,b). The substantial, up to 30%, increase of losses occurs in the area bounded by dispersions of (111) and ($\bar{1}$11) resonances (Figure 2a). Important, that this area is also crossed by a(11) and o(11) SPP modes propagating at air and opal sides of the metal film, respectively (Figure 8b). In the rest of the spectrum pattern the high reflectivity of the metal film prevents light from entering the sample interior that reduces losses compared to that in the uncoated opal.

Thus, we can attribute the increase of losses to the overlap of diffraction resonances in a dielectric lattice and plasmonic resonances. The underlying mechanisms are following. i) The excitation of SPP modes diverts a fraction of the incident light intensity off the zero diffraction order. This diversion results in the deep and broad minimum in the reflectance spectra obtained from the Au side of Au-opal hybrid.[46] ii) The hybridization of Bloch modes of the opal and SPP modes of the Au film improves the conditions for draining the light intensity off the zero diffraction order. Earlier we reported that ($\bar{1}$11) and (200) transmission minima in opal spectra are transformed into transmission bands in Au-opal spectra.[35] Taking into account the close vicinity of dispersion traces of these resonances in the opal lattice to (11)-type SPP resonances in the corrugated metal film (see the example in Figure 8b), the interaction of these

© 2011 WILEY-VCH Verlag GmbH & Co. KGaA, Weinheim

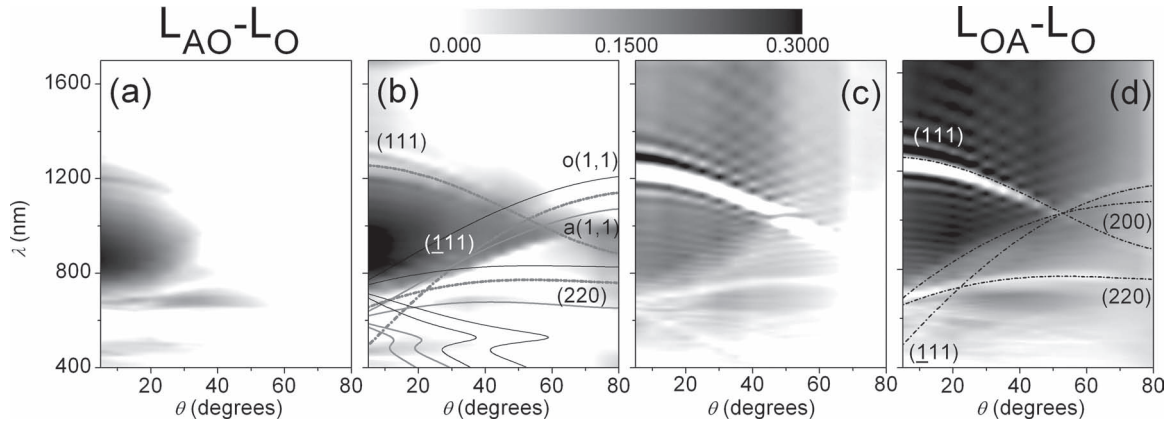

Figure 8. a,b) The differential loss patterns of the Au-opal hybrid crystal along the Au-opal-glass (AO) propagation direction of the light beam for s- and p-polarized light, respectively. c,d) The same along the glass-opal-Au (OA) direction. b) The SPP dispersions at the opal-Au and air-Au interfaces are shown by solid lines. Numbers indicate only the long wavelength diffraction orders. The SPP dispersions at shorter wavelengths are composed by several orders. The dispersion kink corresponds to absorption peak in Figure 6b. Dash-dotted lines show the dispersions of major diffraction resonances in the opal lattice (compare to Figure 2a). The same intensity scale is applied to all panels.

modes is highly probable. These modes represent another channel of in-plane light escape. iii) The localized plasmon resonance in the metal semishells on dielectric spheres[47] scatters the light from the zero diffraction order. This resonance is set at wavelengths somewhat longer, compared to the extraordinary transmission peak occurring at 725 nm for $\theta = 0^{\circ}$.[4] The resonance frequency of a standing alone semishell depends on the ratio of the shell thickness to its diameter, like in spherical nanoshells.[48] Hence, this additional light scattering occurs in the vicinity to (111) diffraction resonance for a given semishell geometry. However, exploiting the localized plasmon resonance is potentially dangerous because it leads to energy dissipation in metal semishells.

The substantial increase of losses is observed compared to the bare opal film if the opal side of the Au-opal hybrid is illuminated (Figure 8c,d). This effect is the direct consequence of the diffractive light diversion in the opal volume that is sourced additionally by the SPP radiative decay and enhanced by reflectivity of the metal film. At diffraction resonances the loss intensity inside the structure decreases, because resonances suppress the light admission inside the PhC. Expectedly, the higher reflectance occurring for the s-polarized light at oblique incidence leads to lower loss magnitude. The two latter observations are the shortcomings related to the opal film ordering.

The re-routing of the incident light flow in the Au-opal hybrid structure is sketched in **Figure 9**a. In the first approximation, the incident light experiences the diffraction in a 3D lattice, which expands the incident beam in a number of diffraction orders propagating in the opal volume along different directions. The metal film acts as a mirror thus confining light and increasing its path length. The evidence of the stronger confinement is the increase of the Fabry–Perot oscillation magnitude (compare Figure 2d and Figure 5c). The bouncing beam promotes further light losses. In turn, each beam that approaches the metal coating is expanded into a series of SPP diffraction orders by 2D hexagonal grating in correspondence to the momentum conservation law (Figure 9b):[49]

$$k(\omega) = \pm\sqrt{k_{\mathrm{SPP}}(\omega)^2 - \left(\frac{2\pi}{D\sqrt{3}}(2j-i)\right)^2} - \frac{2\pi i}{D},\ i, j = 0, \pm 1, \pm 2$$

where $k_{\mathrm{SPP}}(\omega) = \frac{2\pi}{\lambda}\sqrt{\frac{\varepsilon_{\mathrm{d}}\ \varepsilon_{\mathrm{m}}}{\varepsilon_{\mathrm{d}}+\varepsilon_{\mathrm{m}}}}$, ε_{m}, ε_{d} are the dielectric constants of the metal and the dielectric in contact with this metal. Two sets of SPP dispersion branches for the air- and opal-facing interfaces of the metal film, which are spectrally shifted in proportion to the refractive index of each contacting dielectric, should be taken into account. In particular, light coupled to $o(11)$ and $a(11)$ modes can be detected in the loss pattern (Figure 8b). Moreover, in the case of a thin metal film, the SPP modes at opposite interfaces are not independent from each other and this interaction further complicates the scattering process.

Switching from s- to p-polarized light has almost no effect on the differential loss pattern due to 3D diffraction in the opal lattice. The polarization is defined with respect to the plane of incidence. Since the diffraction orders related to different crystal planes propagate in and off the plane of incidence simultaneously, the link between the polarization of the incident light and SPP excitation becomes broken (Figure 9b). Further polarization mixing occurs due to diffraction at the 2D corrugation of the metal film.[50]

Many diffraction orders with short and long tangential projections of their wavevectors are able to reach the metal film. Correspondingly, the guided SPP modes of different in-plane wavevectors can be excited simultaneously for each beam that approaches the metal film at a certain incidence angle (Figure 9c). This multiple light diversion is the reason for smoothing of the loss pattern over different incidence angles.

However, this diversion has some limitations. First of all, the diffraction of the incident beam at (*hkl*) plane in 3D lattice does not produce any new SPP branches compared to its diffraction at the 2D *(hk)* corrugated metal film because one of the indices becomes ineffective, when the (*hkl*) 3D lattice is projected to its surface. Then, one has to take into account that opal possesses a regular structure just in average. The same disorder

© 2011 WILEY-VCH Verlag GmbH & Co. KGaA, Weinheim

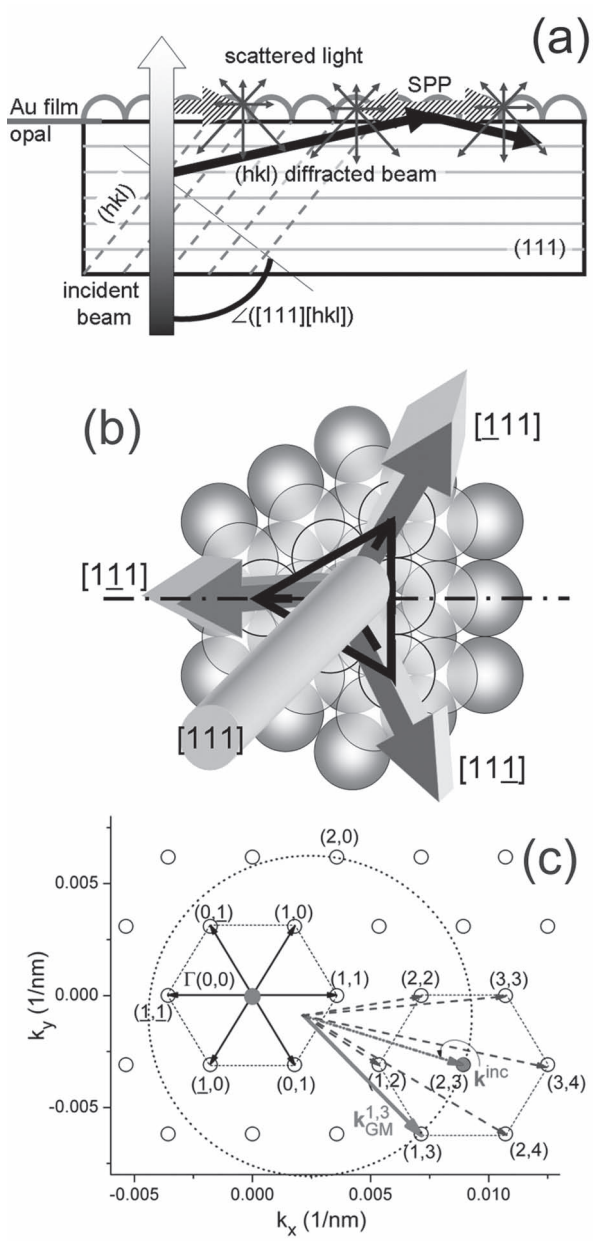

Figure 9. a) Schematics depicting the excitation of SPPs in the Au film on the PhC surface by the incident and diffracted beams and following radiative decay of SPPs. The reflectance of this structure does not obey reciprocity with respect to reversing the beam propagation direction in contrast to the transmission. b) Illustration of the depolarization of the p-polarized incident beam due to diffraction at {111} planes of the 3D opal lattice. Bars at arrows indicate the E-vector of the EM field. Dash-dotted line depicts the plane of incidence. c) The reciprocal lattice of the 2D plasmonic crystal at the opal surface. Dotted hexagons indicate the lattice vectors that correspond to the long range periodicity in the real space. k^{inc} is the wavevector of the oblique incident light (dash-doted line). The guided SPP modes are shown by solid arrows. For the modes shown by dashed arrows the condition of phase synchronism is not fulfilled. The six SPPs diffractively coupled to the incident beam at normal incidence $k^{inc} = 0$ ((point Γ) contrasts the one SPP mode with $k^{1,3}_{GM}$ excited by the incident beam with $k^{inc} \neq 0$ tangential projection, while the same vectors of the reciprocal lattice are involved in coupling. The ring is the trace of the Ewald sphere.

is translated to the 2D metal corrugation. Hence, the most efficient coupling is provided by the shortest vectors of its reciprocal lattice. Correspondingly, the incident waves with long tangential projections of their wavevectors are less efficient in terms of SPP excitation (Figure 9c). This consideration explains the decrease of loss intensity along the incidence angle increase in Figure 8.

The reverse process, the radiative decay of SPP modes, exploits the same reciprocal lattice for diffractive outcoupling. As a result, the propagation of coherently scattered light is equalized over all directions allowed by the momentum conservation law. Thus, the fully deterministic mechanism of diffractive coupling–decoupling of SPPs in hybrid plasmonic-photonic crystals accomplishes the aim of spreading the incident light and, correspondingly, increasing the dwell time of photons inside such architectures. Further homogenization of the scattered light pattern is provided by the random scattering at inhomogeneities of the opal lattice.

6. Light Losses Due to Heterostructuring

In studied heterocrystals the (2 + 1)D LB crystal[51] was used as the counterpart to the 3D opal crystal (Figure 1d). Assembling the LB crystal on top of the Au-opal hybrid results in substantial increase of losses in the LB-Au-opal heterostructure under s-polarized illumination (**Figure 10**a). Somewhat weaker loss enhancement is achieved for the p-polarized light (Figure 10b).

The functions performed by the LB film in this architecture are manifold. Firstly, the effective refractive index of the LB film is low, $n_{effLB} \sim 1.28$, hence, the weak refraction almost preserves the direction of oblique light propagation inside the structure and reduces the reflectance (Figure 4a).[52] Secondly, assembling of the LB film on the metal film with unmatched corrugation profile brings plenty of defects, the relative size of which is small compared to the wavelength. Such defects produce isotropic light scattering,[1] moreover, the metal mirror returns back its forward scattered component. This random scattering mechanism becomes more efficient at the long wavelength range and at grazing light incidence. The result is the milky appearance of the LB-Au-opal sample as it is seen from the LB film-coated side. Thirdly, the LB film applies grating coupling conditions to SPPs in the metal film that are different from those provided by the opal periodicity. Such overlaying perturbation profile stimulates the radiative collapse of SPPs (**Figure 11**). Fourthly, the stop-band of the LB crystal overlaps the extraordinary transmission band of the Au-opal hybrid thus counteracting the transmission increase and the corresponding loss decrease. The latter effect was achieved by purposive choice of the sphere size in the LB film.

Another mechanism of the scattering enhancement relates to the PBG mismatch between the opal and the LB films of the heterocrystal. Since the hetero-PhC consists of two PhCs with different PBG structures,[53,54] this makes unlikely the seamless light propagation across the interface. For the reason that the EM field at both sides of the interface is transported by Bloch modes having different spatial distributions of the field, the coupling is inefficient. Therefore, the light that advances the interface has to be scattered in the first place and, consequently, the field of matched symmetry will be selected from diffuse

© 2011 WILEY-VCH Verlag GmbH & Co. KGaA, Weinheim

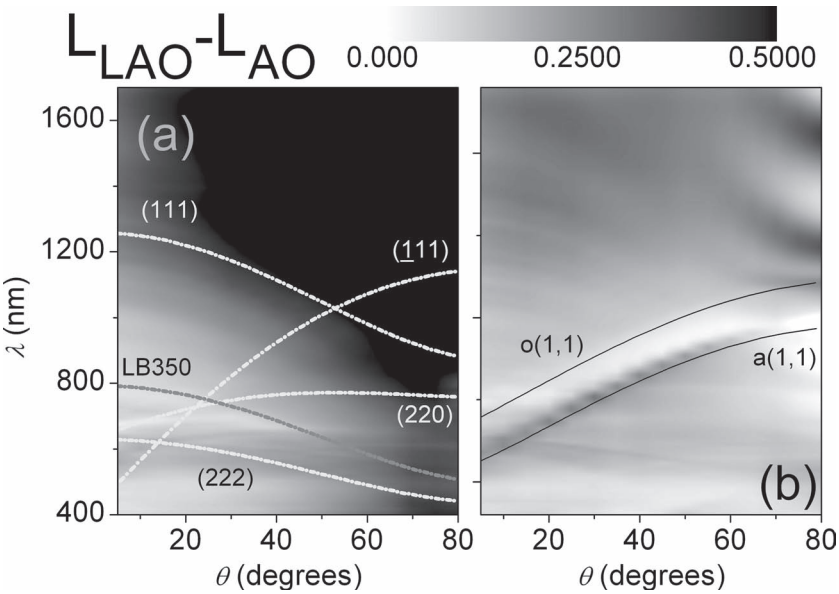

Figure 10. The differential loss patterns of the LB-Au-opal (LAO) hybrid crystal relative to the Au-opal (AO) hybrid. LAO is illuminated on the LB film side and AO–on the metal film side with (a) s- and (b) p-polarized light. Dash-dotted lines show the dispersions of diffraction resonances in the opal lattice and the dispersion of the diffraction resonance in the LB film (LB350). The same intensity scale is applied to both panels. The SPP dispersions at the opal-Au and air-Au interfaces are shown in the panel (b). Numbers at curves indicate the diffraction orders.

light and coupled to another PhC. The need of mode matching forces the interface to source the uncoupled light.[54]

Thus the random and PBG heterointerface-related scattering mechanisms in LB-Au-opal hybrid heterocrystal act together with the diversion mechanisms based on SPP coupling–decoupling in a corrugated metal film and on diffraction in the PhC lattice (Figure 11). Since these mechanisms possess the different origins, they reimburse the shortcomings of each other, such as the limited spectral range, the polarization dependence and the directionality.

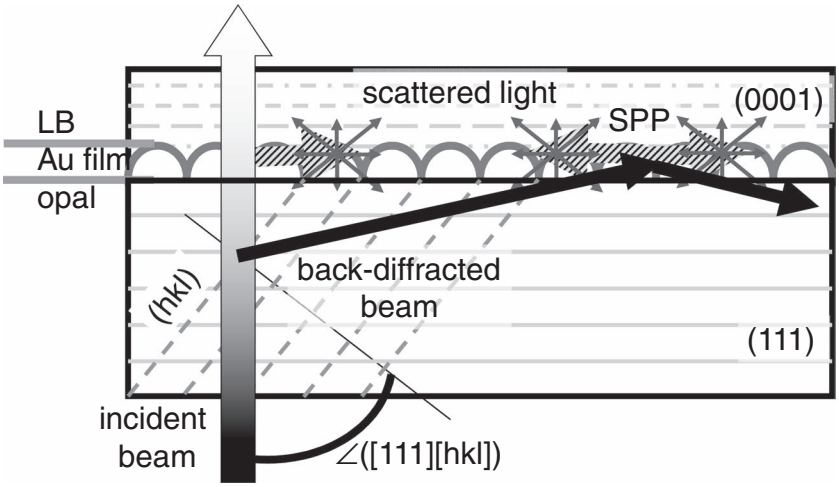

Figure 11. Schematics illustrating the SPP coupling to incident and diffracted in a PhC beams and following radiative decay of these SPPs similarly to Figure 9a. Note, that the coupling of the radiatively decaying SPP waves to the free space is reduced by the PhCs on both sides of the metal film.

7. Conclusions

The hybrid architecture consisting of photonic and plasmonic crystals achieves its outmost diversion of the incident light, when the continuous corrugated metal film is deposited on the interface between two photonic crystals with different lattices. In such structure the broadband $\Delta\lambda/\lambda_{\text{center}} \approx 100\%$, omnidirectional and polarization insensitive diverting of more than 90% of the incident light intensity has been observed.

The most prominent physical mechanisms behind the molding of the light flow in hybrid architectures are the light diffraction in 3D PhC, the light coupling to short living surface plasmon polaritons and scattering at the interface of the heterocrystal.

It should be emphasized that the efficiency of light scattering in hybrid heterocrystals can be easily overestimated, especially at shorter wavelengths, where the light absorption in a metal film cannot be neglected. We calculated losses from the decrease of light intensity in the zero diffraction order instead of measuring the actual light intensity off the zero order path, since the latter method requires much more tedious measurements. We plan to compare these quantities in the future to estimate the fraction of absorbed light in total losses.

It is worth noting that high losses were achieved at the cost of relatively large thickness of the structure that exceeds the operation wavelength by a factor of 10. This factor can be reduced by 3–4 times using the PhCs of high refractive contrast, e.g., using the silicon or rutile replicas of colloidal crystals.

One possible application of the studied architecture is in photovoltaics. If we assume that amorphous Si is embedded in interstitials, the convolution of the absorption spectrum of the semiconductor, the standard sunlight spectrum and the loss spectra integrated over all incidence angles for both light polarizations produce the measure of the trapping efficiency. These numbers scale as 71% of absorbed incident sun radiation in the spectral range from 400 to 1600 nm for bare opal film, 71 and 80% – for the LB-opal heterocrystal illuminated from the opal and LB side, 81 and 65% – for the Au-opal hybrid illuminated from the opal and the metal film sides, and 92 and 83% – for the LB-Au-opal hybrid illuminated from the LB and the opal sides, respectively. Taking into account that rapid decrease of the a-Si absorption at $\lambda > 900$ nm down to nothing at $\lambda > 1200$ nm, the above

© 2011 WILEY-VCH Verlag GmbH & Co. KGaA, Weinheim

numbers underestimate trapping itself, but nevertheless show the progress in trapping efficiency.

Important, that for accomplishing the functionality concerned the requirements for the ordering of the colloidal crystal lattice are not exceptionally high, which in practice allows one to use fast methods of colloidal crystallization. The use of the PhC as a template for metal evaporation then avoids the need for lithography to form a corrugated metal film. Moreover, matching the photonic and plasmonic modes in this architecture is always achieved because of the way the material is fabricated.

8. Experimental Section

Opal films were crystallized on hydrophilic microscope glass slides from a suspension of poly-methyl methacrylate (PMMA) spheres with the diameter $D = 560$ nm and index of refraction $n_{PMMA} = 1.489$ using a procedure described elsewhere.[41,55] In order to prevent the opal erosion during the course of further processing, a 10-nm-thick layer of Al_2O_3 was deposited on the inner surface of the opal voids by atomic layer deposition using trimethylaluminium and water as precursors. The thickness of thin film opal crystals was 5–8 µm.

A nominally 50-nm-thick Au film was sputtered on top of freshly crystallized opal film (Figure 1c). The heterocrystals were assembled by depositing 10 monolayers of silica spheres of 350 nm in diameter on top of the gold film using the Langmuir–Blodgett (LB) method.[56,57] The LB film thickness was ~3 µm. The overall thickness of heterofilms was about 6–10 µm and the covered area was 2–4 cm^2. A scanning electron microscopy (SEM) image of the resulting heterofilm gives an overview of the studied hybrid heterostructure (Figure 1d).

Reference samples–the opal and the LB films, which are comparable to the films composing the heterostructure, were prepared using the same procedures and from the same spheres. Remarkably, the LB-Au-opal hybrid heterocrystals acquire a milky appearance, whereas the colloidal crystal films comprising the heterostructure are highly transparent. This is the direct evidence of the intense scattering occurring in the purposively designed architecture.

Angle-resolved transmission/reflectance spectroscopy with a resolution of 1° was used to investigate in details the optical response of these architectures at different angles, θ, from 0° (5° in the case of reflectance) to 80°, of the beam incidence with respect to the film normal. The samples were illuminated by white light from a tungsten lamp. The incident light was collimated to a beam of ~1 mm in diameter. The spectra were acquired using s- and p-polarized light, the electrical field vectors of which are oriented perpendicular and parallel to the plane of light incidence, respectively. A quarter-wave plate was used to convert the light into circular polarized one before approaching the spectrometer to avoid any polarization dependence caused by the spectrometer grating. The plane of the light incidence was oriented in a way to scan along the high-symmetry cross-section in the opal reciprocal lattice. The transmission and reflectance spectra of samples were measured along direct and reverse directions of light propagation.

Acknowledgements

AVK, UP and SGR are grateful to DFG Cluster of Excellence "Engineering of Advanced Materials" (Germany) for financial support, BD and SGR were supported by the SFI RFP PHY076 grant (Ireland). M.B. and M.P. acknowledge support from SFI grant PI 07/IN.1/1787 (Ireland). Both groups are linked through the COST Action MP0702
Note: This article was amended on November 8, 2011 to update Figure 9b which was incorrect in the version first published online.

Received: March 29, 2011
Revised: August 17, 2011
Published online: September 26, 2011

[1] H. C. Van De Hulst, *Light Scattering by Small Particles*, Dover, **1982.**
[2] P. Bermel, C. Luo, L. Zeng, L. C. Kimerling, J. D. Joannopoulos, *Opt. Express* **2007**, *15*, 16986.
[3] H. A. Atwater, A. Polman, *Nat. Mater.* **2010**, *9*, 205.
[4] S. G. Romanov, A. Regensburger, A. V. Korovin, U. Peschel, *Adv. Mater.* **2011**, *23*, 2515.
[5] D. Zhou, R. Biswas, *J. Appl. Phys.* **2008**, *103*, 093102.
[6] B. Curtin, R. Biswas, V. Dalal, *Appl. Phys. Lett.* **2009**, *95*, 231102.
[7] D. Duche´, L. Escoubas, J.-J. Simon, P. Torchio, W. Vervisch, F. Flory, *Appl. Phys. Lett.* **2008**, *92*, 193310.
[8] J. R. Tumbleston, D.-H. Ko, E. T. Samulski, R. Lopez, *Appl. Phys. Lett.* **2009**, *94*, 043305.
[9] J. R. Tumbleston, D.-H. Ko, E. T. Samulski, R.Lopez, *Opt. Express* **2009**, *17*, 7670.
[10] C. Ulbrich, S. Fahr, J. Üpping, M. Peters, T. Kirchartz, C. Rockstuhl, R. Wehrspohn, A. Gombert, F. Lederer, U. Rau, *Phys. Status Solidi A* **2008**, *205*, 2831.
[11] J. C. Goldschmidt, M. Peters, L. Prönneke, L. Steidl, R. Zentel, B. Bläsi, A. Gombert, S. Glunz, G. Willeke1, U. Rau, *Phys. Status Solidi A* **2008**, *205*, 2811.
[12] A. Chutinan, S. John, *Phys. Rev. A* **2008**, *78*, 023825.
[13] F. Hallermann, C. Rockstuhl, S. Fahr, G. Seifert, S. Wackerow, H. Graener, G. v. Plessen, F. Lederer, *Phys. Status Solidi A* **2008**, *205*, 2844.
[14] H. A. Atwater, A. Polman, *Nat. Mater.* **2010**, *9*, 205.
[15] C. F. Bohren, *Am. J. Phys.* **1983**, *51*, 323.
[16] C. Dahmen, G. von Plessen, *Aust. J. Chem.* **2007**, *60*, 447.
[17] S. A. Maier, *Plasmonics: Fundamentals and Applications;* Springer, New York, **2007**.
[18] A. Otto, *Z. Phys.* **1968**, *216*, 398.
[19] E. Kretschmann, H. Raether, *Z. Naturforsch. A* **1968**, *23*, 2135.
[20] R. H. Ritchie, E. T. Arakawa, J. J. Cowan, R. N. Hamm, *Phys. Rev. Lett.* **1968**, *21*, 1530.
[21] N. L. Dmitruk, A. V. Korovin, S. V. Mamykin, M. V. Sosnova, E. F. Venger, *Ukr. J. Phys.* **2009**, *54*, 559.
[22] V. E. Ferry, L. A. Sweatlock, D. Pacifici, H. A. Atwater, *Nano Lett.* **2008**, *8*, 4391.
[23] a) K. R. Catchpole, A. Polman, *A. Opt. Express* **2008**, *16*, 21793; b) R. A. Pala, J. White, E. Barnard, J. Liu, M. L. Brongersma, *Adv. Mater.* **2009**, *21*, 3504.
[24] L. S. Roman, O. Inganas, T. Granlund, T. Nyberg, M. Svensson, M. R. Andersson, J. C. Hummelen, *Adv. Mater.* **2000**, *12*, 189.
[25] C. Cocoyer, L. Rocha, L. Sicot, B. Geffroy, R. de Bettignies, C. Sentein, C. Fiorini-Debuisschert, P. Raimond, *Appl. Phys. Lett.* **2006**, *88*, 133108.
[26] S.-I. Na, S.-S. Kim, J. Jo, S.-H. Oh, J. Kim, D.-Y. Kim, *Adv. Funct. Mater.* **2008**, *18*, 3956.
[27] S. Mokkapati, F. J. Beck, A. Polman, K. R. Catchpole, *Appl. Phys. Lett.* **2009**, *95*, 53115.
[28] V. G. Balakirev, V. N. Bogomolov, V. V. Zhuravlev, Y. A. Kumzerov, V.P. Petranovskii, S. G. Romanov, L. A. Samoilovich, *Crystallogr. Rep.* **1993**, *38*, 348.
[29] T. Beckers, J. Üpping, A. Bielawny, A. Lambertz, B. Stannowski, R. Carius, R. B. Wehrspohn, *Proc. 25 Europ. Photovoltaic Solar Energy Conf.* **2010**, 3073.
[30] P. G. O'Brien, A. Chutinan, K. Leong, N. P. Kherani, G. A. Ozin, S. Zukotynski, *Opt. Express* **2010**, *18*, 4478.
[31] A. Mihi, F. J. López-Alcaraz, H. Míguez, *Appl. Phys. Lett.* **2006**, *88*, 193110.
[32] C. L. Huisman, J. Schoonman, A. Goossens, *Sol. Energy Mater. Sol. Cells* **2005**, *85*, 115.
[33] Z. Zhou, X. S. Zhao, *Langmuir*, **2005**, *21*, 4717.
[34] B. Ding, M. Bardosova, I. Povey, M. E. Pemble, S. G. Romanov, *Adv. Funct. Mater.* **2010**, *20*, 853.

© 2011 WILEY-VCH Verlag GmbH & Co. KGaA, Weinheim

[35] B. Ding, M. E. Pemble, A. V. Korovin, U. Peschel, S. G. Romanov, *Phys. Rev. B* **2010**, *82*, 035119.
[36] A.-L. Baudrion, J.-C. Weeber, A. Dereux, G. Lecamp, P. Lalanne, S. I. Bozhevolnyi, *Phys. Rev. B* **2006**, *74*, 125406.
[37] T. W. Ebbesen, H. J. Lezec, H. F. Ghaemi, T. Thio, P. A. Wolff, *Nature* **1998**, *391*, 667.
[38] L. Landstrom, D. Brodoceanu, D. Bauerle, F. J. Garcia-Vidal, S. G. Rodrigo, L. Martin-Moreno, *Optics Express* **2009**, *17*, 761.
[39] W. L. Barnes, A. Dereux, T. W. Ebbesen, *Nature* **2003**, *424*, 824.
[40] B. Ding, M. E. Pemble, M. Bardosova, A. V. Korovin, U. Peschel, S. G. Romanov, *Proc. SPIE*, (Eds. H. Migues, C. Seassal, L. Andreani, S.G. Romanov), **2010**, *7713*, 771304.
[41] W. Khunsin, G. Kocher, S. G. Romanov, C. M. Sotomayor Torres, *Adv. Funct. Mat.* **2008**, *18*, 2471.
[42] S. G. Romanov, *J. Appl. Phys.* **2008**, *103*, 093117.
[43] S. G. Romanov, U. Peschel, M. Bardosova, S. Essig, K. Busch, *Phys. Rev. B* **2010**, *82*, 115403.
[44] B. R. Cooper, H. Ehrenreich, H. R. Philipp, *Phys. Rev.* **1965**, *138*, 494 A.
[45] I. Ursu, I. N. Mihailescu, A. M. Prokhorov, V. I. Konov, V. N. Tokarev, *Physica C* **1985**, *132*, 395.
[46] B. Ding, M. E. Pemble, A. V. Korovin, U. Peschel, S. G. Romanov, *Appl. Phys. A* **2011**, *103*, 889
[47] A. I. Maaroof, M. B. Cortie, N. Harris, L. Wieczorek, *Small* **2008**, *4*, 2292.
[48] E. Prodan, P. Nordlander, N. J. Halas, *Nano Lett.* **2003**, *3*, 1411.
[49] H. F. Ghaemi, T. Thio, D.E. Grupp, T. W. Ebbesen, H. J. Lezec, *Phys. Rev B* **1998**, *58*, 6779.
[50] T. D. Backes, D. S. Citrin, *IEEE J. Sel. Top. Quantum Electron.* **2008**, *14*, 1530.
[51] S. G. Romanov, M. Bardosova, D. E. Whitehead, I. Povey, M. Pemble, C.M. Sotomayor Torres, *Appl. Phys. Lett.* **2007**, *90*, 133101.
[52] D. Han, X. Li, F. Wu, X. Liu, J. Zi, *Appl. Phys. Lett.* **2006**, *88*, 161110.
[53] S.G. Romanov, H.M. Yates, M.E. Pemble, R.M. De La Rue, *J.Phys.:Cond.Matter.* **2000**, *12*, 8221.
[54] E. Istrate, E. H. Sargent, *Rev. Mod. Phys.* **2006**, *78*, 455.
[55] M. Müller, R. Zentel, T. Maka, S. G. Romanov, C. M. Sotomayor Torres, *Chem. Materials* **2000**, *12*, 2508.
[56] M. Bardosova, P. Hodge, L. Pach, M. E. Pemble, V. Smatko, R. H. Tredgold, D. Whitehead, *Thin Sol. Films* **2003**, *437*, 276.
[57] S. Reculusa, S. Ravaine, *Chem. Mater.* **2003**, *15*, 598.

© 2011 WILEY-VCH Verlag GmbH & Co. KGaA, Weinheim